Unified Time and Frequency Picture of Ultrafast Atomic Excitation in Strong Laser Fields

H. Zimmermann,[1,*] S. Patchkovskii,[1,†] M. Ivanov,[1,2,3] and U. Eichmann[1,‡]
[1]Max-Born-Institut, Max-Born-Str. 2A, 12489 Berlin, Germany
[2]Department of Physics, Humboldt University, Newtonstrasse 15, 12489 Berlin, Germany
[3]Blackett Laboratory, Imperial College London, South Kensington Campus, SW7 2AZ London, United Kingdom
(Received 11 August 2016; published 5 January 2017)

Excitation and ionization in strong laser fields lies at the heart of such diverse research directions as high-harmonic generation and spectroscopy, laser-induced diffraction imaging, emission of femtosecond electron bunches from nanotips, self-guiding, filamentation and mirrorless lasing during propagation of light in atmospheres. While extensive quantum mechanical and semiclassical calculations on strong-field ionization are well backed by sophisticated experiments, the existing scattered theoretical work aiming at a full quantitative understanding of strong-field excitation lacks experimental confirmation. Here we present experiments on strong-field excitation in both the tunneling and multiphoton regimes and their rigorous interpretation by time dependent Schrödinger equation calculations, which finally consolidates the seemingly opposing strong-field regimes with their complementary pictures. Most strikingly, we observe an unprecedented enhancement of excitation yields, which opens new possibilities in ultrafast strong-field control of Rydberg wave packet excitation and laser intensity characterization.

DOI: 10.1103/PhysRevLett.118.013003

If one endeavors to comprehend atomic strong-field physics one has to be prepared to be a restless wanderer between two worlds: the multiphoton and the tunneling realms. Thereby, the Keldysh parameter γ [1] serves as a faithful, but rather vague guide in which region a particular experiment resides. Both domains provide their own convincing notions on how to understand the underlying physics at least qualitatively. While the tunneling picture concentrates on time aspects [2–4], the multiphoton world, which shines through whenever experimental observations suggest resonance effects to be responsible for enhanced features [5–7], rests on a complementary approach in the frequency domain. Since Keldysh's work [1], the two regimes have been clearly delineated as the two limits $\gamma < 1$ for tunneling and $\gamma > 1$ for multiphoton. Strong-field excitation of atoms has been initially observed in the multiphoton regime [8–10]. Thereby, the excitation has been almost solely associated with the multiphoton picture, no matter what regime the Keldysh parameter suggests. Only recently, strong-field excitation in the tunneling regime has been measured and successfully described by the frustrated tunneling ionization (FTI) model [11], offering a time dependent perspective on excitation. Moreover, recent investigations on atomic strong-field excitation and acceleration [12] at intensities beyond saturation have given strong hints of the existence of long sought bound states of a nearly free electron in strong laser fields [13], known as Kramers-Henneberger states [14], and have uncovered unexpected links of strong-field excited states to nonlinear phenomena such as the high order Kerr effect [15], high-harmonic generation [16], and multiphoton Rabi oscillations [17]. Despite its newly recognized importance, however, the existing scattered theoretical work [18,19] aiming at a full quantitative understanding of strong-field excitation lacks experimental confirmation.

In this Letter we present experiments on strong-field excitation of rare gas atoms in both the tunneling and multiphoton regime and their interpretation based on time dependent Schrödinger equation (TDSE) calculations. Particularly, in our analysis we will concentrate on the signatures of channel closing [20,21], a genuine multiphoton effect (or more precisely, an effect of the time-periodicity of the driving field), in the excitation and their evolution through the two regimes, from multiphoton to tunneling. We mainly address high-n Rydberg states in the vicinity of a channel closing, which have Kepler orbital periods much larger than the laser pulse duration and, therefore, cannot be considered resonances. This property separates the quasicontinuum of Rydberg states from the well-known Freeman resonances [5], which have Kepler orbital periods less than the laser pulse duration.

In the *multiphoton* picture channel closings originate from the ponderomotive shift $U_p = (F_0^2/4\omega^2)$ (atomic units are used throughout, unless specified otherwise) of the ionization continuum, where F_0 is the peak electric field (peak intensity $I \propto F_0^2$) and ω is the laser frequency. An m-photon ionization channel closes when $m\omega \leq I_p + U_p$; i.e., the combined energy of m photons falls below the upshifted continuum threshold (I_p is the ionization potential). The closing decreases the ion yield in the m-photon channel. On the other hand, the underlying resolved [5] or unresolved quasicontinuum of Rydberg states shifts into resonance [18,19]. Depending on the ionization rate of these

intermediate (transient) resonances, the yield in the $m+1$ channel may, in fact, increase, as was shown in pioneering ATI experiments [5,7] and later confirmed in calculations [6,7,22]. If, on the other hand, excited states are stabilized by the intense field [13,18,19,23], accumulation of the excited states should result. This modulation of the excitation cross section in the vicinity of a channel closing has not been observed in strong-field experiments so far.

In the *time-domain* picture channel closings arise as a destructive interference between electron bursts liberated at subsequent peaks of the laser field. The gross structure of these interferences is transparent within the strong-field approximation (SFA). The SFA amplitude a_p for the direct photoelectron with momentum p can be written as a sum over stationary trajectories [24,25]:

$$a_p = \sum_{t_s} a_{\mathrm{prop}}(p, t_s) a_{\mathrm{ion}}(p, t_s) \tag{1}$$

where a_{ion} is a strong-field ionization amplitude. The sum is over all stationary times t_s, which are repeated for each laser cycle. For a slowly varying pulse envelope, the dominant time-dependent contribution in Eq. (1) comes from the propagation amplitude $a_{\mathrm{prop}} \propto \exp(i\phi_s)$, where the stationary phase ϕ_s is

$$\phi_s = -\frac{1}{2} p^2 (T - t_b) + I_p t_b - \int_{t_b}^{T} U_p(t) dt. \tag{2}$$

Here, T is the observation time, $t_b = \Re(t_s)$ is the ionization time, and $U_p(t)$ is the cycle average of the quiver energy. For two trajectories born at subsequent laser cycles to interfere constructively, the phases ϕ_s must differ by a multiple of 2π, leading to the condition,

$$I_p + U_p + \frac{1}{2} p^2 = m\omega. \tag{3}$$

Setting the photoelectron momentum to zero then yields the closure condition for the m-photon ionization channel. We note that this approach is also suitable for describing strong-field excitation, since the low momentum electrons are known to be partially recaptured by the Coulomb potential into excited Rydberg states through FTI [11].

In the experiment we investigate strong-field excitation of Ar and Ne atoms by 800 and 400-nm laser fields, with intensities up to 10^{16} and 2×10^{15} W cm^{-2}, respectively. The experimental setup is outlined in Fig. 1 (see also Supplemental Material [26]). We emphasize that we measure the yield of strong field-excited atoms, rather than ions. The measured yields of excited atoms are summarized in Fig. 2. The most prominent feature of the experimental data is the sequence of steps found in the Ar* yield at 400 nm [panel (a)]. The $(90 \pm 20)\times$ increase between 175 and 275 TW cm^{-2} is clearly associated with the closing of

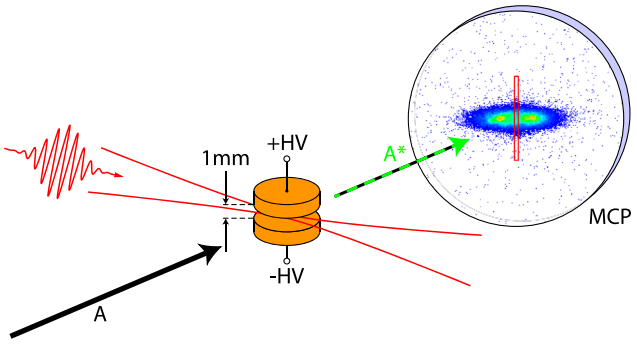

FIG. 1. Sketch of the experimental setup. A focused linearly polarized laser beam with a pulse duration of 45 fs full width at half maximum and a center wavelength of either 800 or 400 nm intersects a collimated effusive beam of rare gas atoms midway between two field plates, where high voltages (HV) can be applied for pulsed field ionization (see Supplemental Material [26]). The atomic beam A is directed towards a position-sensitive multichannel plate (MCP) detector, which detects excited atoms A* due to their high internal energy (≈10 eV or more). Ground state atoms are not detected. A typical distribution of excited atoms is shown color coded. For the analysis we take only signals stemming from the immediate vicinity of the focal plane (red rectangle) to reduce volume-averaging effects.

the six-photon ionization channel, which occurs at 190 TW cm^{-2} [black arrows, top of Fig. 2(a)]. A less pronounced $(5 \pm 3)\times$ increase between 40 and 70 TW cm^{-2} can be tentatively assigned to a five-photon resonance with the Stark-shifted $3p^5 6s^1$ manifold of Ar based on TDSE results. For Ne, the first (seven-photon) channel closing is expected to occur already at 8 TW cm^{-2}, too low for ionization or excitation to be detected in our apparatus. The eight- and nine-photon channels close respectively at 218 and 428 TW cm^{-2} [green arrows, bottom of Fig. 2(a)]. Although the density of our intensity grid is insufficient to clearly resolve the steps in Ne* yield, we do see a $(15 \pm 5)\times$ increase between 220 and 270 TW cm^{-2}, followed by a $(4.4 \pm 0.5)\times$ increase between 380 and 430 TW cm^{-2}. We note that the experimental results include focal averaging. The appearance of steps in the focal-averaged results inevitably correlates to a maximum in the intensity-dependent yield before focal averaging (see the Supplemental Material [26]).

Most of the data shown in Fig. 2(a) are obtained in the multiphoton regime $\gamma > 1$ ($\gamma = 1$ at 530 and 720 TW cm^{-2} for Ar and Ne, respectively). It is therefore instructive to examine the excited-atom yield for the 800 nm field [Fig. 2(b)], where tunneling regime $\gamma < 1$ is reached already at 130 TW cm^{-2} for Ar (180 TW cm^{-2} for Ne). For both atoms, a smooth, featureless increase in excited-state yield is seen with increasing intensity. However, the absence of channel-closure steps in our 800 nm data is not conclusive: Channel closings at this wavelength are expected to occur every 26 TW cm^{-2}, while our intensities

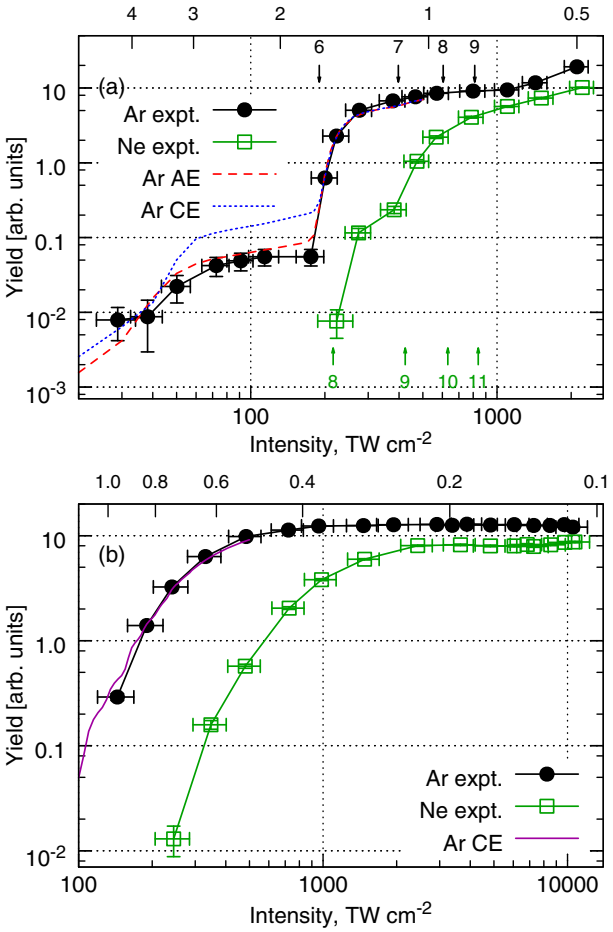

FIG. 2. Yield of strong-field excited Ar (black disks) and Ne (green squares) atoms, as a function the laser intensity (lower x axis). The Keldysh γ parameter for argon is shown on the upper x axis. (a) 400 nm laser wavelength. Volume-averaged TDSE results for the all-electron (AE; red dashed line) and core-eliminated (CE; blue dotted line) model potentials are shown for comparison. Selected channel-closure intensities [$I_m = 3509\omega^2(m\omega - I_p)$, where I_m is in TW cm^{-2}] are indicated by black (Ar, top) and green (Ne, bottom) vertical arrows. (b) 800 nm laser wavelength. Channel closings are found at ≈26 TW cm^{-2} intervals, and are not shown. Experimental intensities are calibrated on the calculated position of the six-photon channel closing in argon.

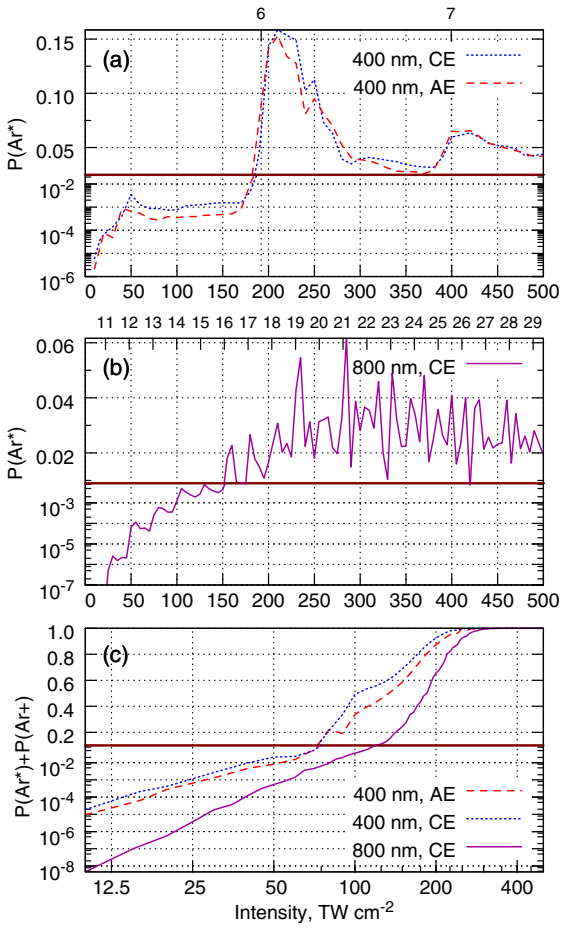

FIG. 3. Probability of ionization and neutral excitation in Ar, as a function of peak intensity (in TW cm^{-2}). Probabilities above (below) brown horizontal line at $P \approx 0.01$ are shown on a linear (logarithmic) scale. (a) Excitation by a 400 nm field. Red dashed line: AE potential; Blue dotted line: CE potential. Intensities of m-photon channel closings are indicated on the top x axis. (b) Probability of neutral excitation in argon for 800-nm driving field. (c) Combined probability of excitation and ionization.

are determined to ≈15% [24 TW cm^{-2} for the lowest intensity shown in Fig. 2(b)]. It nonetheless remains a valid question whether channel-closing signatures persist in the tunneling- and over-the-barrier-ionization regime, and are washed out due to the volume averaging and intensity fluctuations in our experiment. To resolve this important issue, and to further assign the features seen at 400 nm, we turn to numerical simulations.

Our TDSE simulations [31] account for the dynamics of a single active electron (see Supplemental Material [26]). The results from the two model potentials [all-electron (AE) and core-eliminated (CE)] are visually almost indistinguishable in Fig. 3(a). However, the small differences in the excitation probability between 50 and 150 TW cm^{-2} are magnified upon volume averaging. The AE focal spot-averaged result coincides with the experimental curve [Fig. 2(a); red dashed line]. The CE result (blue dotted line) shows excitation-probability steps at the same intensities, but is consistently shifted up by a factor of ≈ 2.5 between 50 and 150 TW cm^{-2}. Since both potentials yield nearly identical results for $I > 150$ TW cm^{-2}, and are qualitatively consistent at all intensities, we exclusively use the CE potential for the 800 nm simulations.

Because of the much smaller channel spacing at 800 nm, the first (11-photon) channel closing is already visible just below ≈25 TW cm^{-2} [Fig. 3(b)]. Regular channel closings are then seen at the expected intensities up to the 17-photon closing (≈180 TW cm^{-2}; 2.7% excitation probability; 52% initial-state survival probability). At higher intensities, the calculated strong-field excitation probabilities remain

strongly modulated (0.7% to 6.2% overall range). At the same time, the positions of the maxima first shift away from the expected channel closings and later become irregular. Focal volume averaging of the calculated excitation probabilities yields an intensity dependence coinciding with the experimental result [Fig. 2(b); solid purple curve], obscuring the modulation of the yield.

The irregular behavior of excitation probability for high-intensity 800 nm pulses is striking, especially when compared to the 400 nm results, which remain regular despite the even higher depletion levels at 400 nm, [Fig. 3(c)]. As a central part of our analysis we explain this pattern in the time domain.

At high depletion levels, both ionization and excitation primarily happen at the raising edge of the pulse, before the peak intensity is reached. Thereby, U_p changes linearly with the intensity between two subsequent cycles. For our 45-fs pulses, the instantaneous intensity increases by 5.5% (400 nm) and 11% (800 nm) between two subsequent cycles at the half of the peak intensity. As a consequence, the electron accumulates an additional phase of $\approx 2\pi(U_p/\omega)R$, where R is defined as the relative intensity change between the two subsequent cycles. For the 400-nm driver, the U_p/ω ratio remains small even at the highest intensity used in our calculations (e.g., $U_p/\omega \approx 2.4$ at $I = 500$ TW cm^{-2}), so that the intensity variation does not affect the positions of channel closings. The situation changes for the 800-nm field: already at $I = 500$ TW cm^{-2}, $U_p/\omega \approx 5.8$. This corresponds to a 1.3π contribution to the continuum phase at the raising edge of the pulse, sufficient to change the sense of the interference between two subsequent cycles from constructive to destructive, and shift the position of the apparent channel closing.

Given the excellent agreement between the calculated and experimental yields, we are encouraged to analyze the calculated Rydberg state populations in the vicinity of the main excitation peak [Fig. 4(a)]. At 180 TW cm^{-2} and 400 nm, right before the raising edge of the peak, the excited-state population distribution is bimodal. The minor contribution around $n = 5$ originates from a five-photon excitation to Stark-shifted $5s$ and $6s$ atomic states. The dominant, broad distribution peaks at $n = 13$ and extends to $n \geq 25$. At this intensity, the six-photon ionization channel is still open. As the intensity increases, the six-photon channel begins to close for high Rydberg states, gradually shifting the population to low n. Beyond 210 TW cm^{-2}, the Rydberg-state distributions become very narrow, and are dominated by individual-state resonances ($5f$, $6f$, and $8f$–$10f$ at 220 TW cm^{-2}; $5f$–$7f$ at 230 TW cm^{-2}; $4f$ at 250 TW cm^{-2}). In the vicinity of the *seven*-photon closing, the pattern repeats itself, although less clearly due to the depletion.

High-n,-l Rydberg states populated at lower intensities are highly resistant to photoionization [19,32], mainly due to a negligible overlap with the atomic core. The survival of

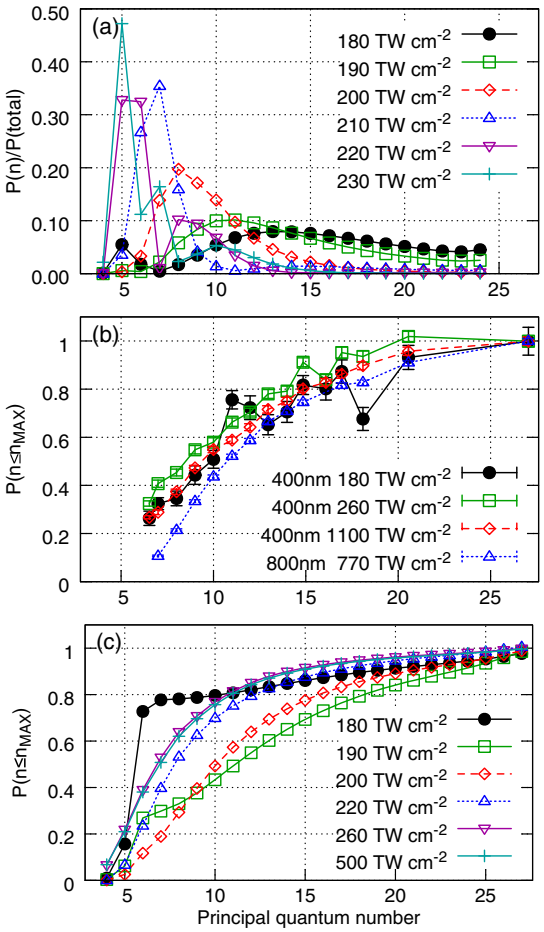

FIG. 4. Distribution of the principal quantum number n of the Rydberg states in Ar after strong-field excitation. Unless noted otherwise, data are for the 400 nm driving field. In (a) the principal quantum number in the abscissa corresponds to n, in (b) and (c) to n_{MAX} (a). Calculated (AE) distributions at different peak intensities close to the six-photon peak in Fig. 3(a). The distributions are normalized to 1 over Rydberg state population with $4 \leq n \leq 23$. The CE distributions are qualitatively similar. (b) Experimental cumulative distributions of n at 180, 260, and 1100 TW cm^{-2} (400 nm) and 770 TW cm^{-2} (800 nm). The error bars include the statistical count error only. (c) Theoretical cumulative distributions after volume averaging.

low-l states, including $l = 0$, suggests that other physical mechanisms (such as interference stabilization [33] or formation of Kramers-Henneberger states [13]) may come into play at the high-intensity side of the excitation peak.

With our experimental setup we are able to extract cumulative n distributions from pulsed field ionization measurements. These could only be measured with sufficient statistics at the high intensity end of the excitation step and at higher laser intensities [Fig. 4(b)]. In spite of low statistics, it appears that the n distribution does shift somewhat towards lower n between 180 (black disks) and 260 TW cm^{-2} (green squares), then moves slightly towards high n again at 1100 TWcm^{-2} (red diamonds).

Interestingly, for all three intensities at 400 nm, a large fraction of states are formed initially in $n \leq 7$ Rydberg states (our static field is insufficient to differentiate between low-n Rydberg states). These patterns are broadly confirmed by the volume-averaged TDSE n distributions [Fig. 4(c)], although the calculated distributions appear to be more sensitive to the peak laser field. Interestingly, the survival probability of low-n states decreases for the 800 nm driving light [Fig. 4(b), blue triangles]. A similar trend is seen in the calculated 800-nm distributions (data not shown). In passing, we also note that at high intensities the FTI model yields very similar n distributions, reflecting the increasingly classical electron motion [34].

In conclusion, we studied strong-field excitation in Ne and Ar in both the multiphoton and tunneling regimes. We have compared the Ar results with TDSE calculations, which are in excellent agreement with the experimental excited atom yield. Deep in the multiphoton regime we were able to directly observe an unprecedented enhancement of the excitation of Rydberg states in the vicinity of a channel closing in Ar and a smaller one in Ne, accessing the hitherto unexplored range of a quasi-continuum of Rydberg states that is responsible for it. The enhancement provides a nearly model-independent intensity calibration. In the tunneling regime resonance effects are strongly modified by the accumulation of the electronic phase in the continuum, making the tunneling picture more intuitively appealing. We emphasize that the analysis thus reconciles the multiphoton and tunneling picture by highlighting the smooth transition from a regular to an irregular excitation pattern at the channel closings, where excitation dominates. We were also able to observe hints of intensity-dependent control of the excited Rydberg state distributions, which are strongly supported by our TDSE results.

M. I. acknowledges support of the DFG QUTIF grant.

*henri.zimmermann@mbi-berlin.de
†serguei.patchkovskii@mbi-berlin.de
‡eichmann@mbi-berlin.de

[1] L. V. Keldysh, Sov. Phys. JETP **20**, 1307 (1965).
[2] T. F. Gallagher, Phys. Rev. Lett. **61**, 2304 (1988).
[3] H. B. van Linden van den Heuvell and H. G. Muller, in *Multiphoton Processes*, edited by S. J. Smith and P. L. Knight (Cambridge University Press, Cambridge, England, 1988).
[4] F. Krausz and M. Ivanov, Rev. Mod. Phys. **81**, 163 (2009).
[5] R. R. Freeman, P. H. Bucksbaum, H. Milchberg, S. Darack, D. Schumacher, and M. E. Geusic, Phys. Rev. Lett. **59**, 1092 (1987).
[6] H. G. Muller, Phys. Rev. Lett. **83**, 3158 (1999).
[7] M. J. Nandor, M. A. Walker, L. D. Van Woerkom, and H. G. Muller, Phys. Rev. A **60**, R1771 (1999).
[8] M. P. de Boer and H. G. Muller, Phys. Rev. Lett. **68**, 2747 (1992).
[9] R. R. Jones, D. W. Schumacher, and P. H. Bucksbaum, Phys. Rev. A **47**, R49 (1993).
[10] L. Fechner, N. Camus, A. Krupp, J. Ullrich, T. Pfeifer, and R. Moshammer, Phys. Rev. A **92**, 051403 (2015).
[11] T. Nubbemeyer, K. Gorling, A. Saenz, U. Eichmann, and W. Sandner, Phys. Rev. Lett. **101**, 233001 (2008).
[12] U. Eichmann, T. Nubbemeyer, H. Rottke, and W. Sandner, Nature (London) **461**, 1261 (2009).
[13] F. Morales, M. Richter, S. Patchkovskii, and O. Smirnova, Proc. Natl. Acad. Sci. U.S.A. **108**, 16906 (2011).
[14] W. C. Henneberger, Phys. Rev. Lett. **21**, 838 (1968).
[15] M. Richter, S. Patchkovskii, F. Morales, O. Smirnova, and M. Ivanov, New J. Phys. **15**, 083012 (2013).
[16] T. Bredtmann, S. Chelkowski, A. D. Bandrauk, and M. Ivanov, Phys. Rev. A **93**, 021402 (2016).
[17] M. Fushitani, C.-N. Liu, A. Matsuda, T. Endo, Y. Toida, M. Nagasono, T. Togashi, M. Yabashi, T. Ishikawa, Y. Hikosaka, T. Morishita, and A. Hishikawa, Nat. Photonics **10**, 102 (2016).
[18] E. Volkova, A. Popov, and O. Tikhonova, J. Exp. Theor. Phys. **113**, 394 (2011).
[19] Q. Li, X.-M. Tong, T. Morishita, H. Wei, and C. D. Lin, Phys. Rev. A **89**, 023421 (2014).
[20] C. Y. Tang, H. C. Bryant, P. G. Harris, A. H. Mohagheghi, R. A. Reeder, H. Sharifian, H. Tootoonchi, C. R. Quick, J. B. Donahue, S. Cohen, and W. W. Smith, Phys. Rev. Lett. **66**, 3124 (1991).
[21] G. G. Paulus, F. Grasbon, H. Walther, R. Kopold, and W. Becker, Phys. Rev. A **64**, 021401 (2001).
[22] J. Wassaf, V. Véniard, R. Taïeb, and A. Maquet, Phys. Rev. A **67**, 053405 (2003).
[23] A. V. Bogatskaya, E. A. Volkova, and A. M. Popov, Laser Phys. **26**, 015301 (2016).
[24] S. V. Popruzhenko, J. Phys. B **47**, 204001 (2014).
[25] O. Smirnova and M. Ivanov, in *Attosecond and XUV Physics: Ultrafast Dynamics and Spectroscopy*, edited by T. Schultz and M. Vrakking (Wiley, New York, 2014).
[26] See Supplemental Material at http://link.aps.org/supplemental/10.1103/PhysRevLett.118.013003 for details on the experimental setup, the TDSE calculations, and the focal-volume averaging, which includes Refs. [27–30].
[27] T. Gallagher, *Rydberg Atoms* (Cambridge University Press, Cambridge, England, 1994).
[28] H. G. Muller, Phys. Rev. A **60**, 1341 (1999).
[29] F. Morales, T. Bredtmann, and S. Patchkovskii, J. Phys. B **49**, 245001 (2016).
[30] D. E. Manolopoulos, J. Chem. Phys. **117**, 9552 (2002).
[31] S. Patchkovskii and H. Muller, Comput. Phys. Commun. **199**, 153 (2016).
[32] U. Eichmann, A. Saenz, S. Eilzer, T. Nubbemeyer, and W. Sandner, Phys. Rev. Lett. **110**, 203002 (2013).
[33] A. M. Popov, O. V. Tikhonova, and E. A. Volkova, J. Phys. B **36**, R125 (2003).
[34] H. Zimmermann, J. Buller, S. Eilzer, and U. Eichmann, Phys. Rev. Lett. **114**, 123003 (2015).